Materials Letters 253 (2019) 276–280

Contents lists available at ScienceDirect

Materials Letters

journal homepage: www.elsevier.com/locate/mlblue

Surface morphology evolution of a polycrystalline diamond by inductively coupled plasma reactive ion etching (ICP-RIE)

Yuting Zheng [a,b], Haitao Ye [b,*], Jinlong Liu [a], Junjun Wei [a], Liangxian Chen [a], Chengming Li [a,*]

[a] Institute for Advanced Materials and Technology, University of Science and Technology Beijing, Beijing 100083, PR China
[b] Department of Engineering, University of Leicester, Leicester LE1 7RH, UK

ARTICLE INFO

Article history:
Received 12 March 2019
Received in revised form 15 June 2019
Accepted 25 June 2019
Available online 26 June 2019

Keywords:
Polycrystalline diamond
Plasma etching
X-ray techniques
Raman
Structural

ABSTRACT

The needle-like surface morphology evolution in oxygen plasma in combination with a secondary gas (Cl_2, CHF_3 or CF_4) by inductively coupled plasma reactive ion etching (ICP-RIE) on a free-standing polycrystalline diamond was investigated. The addition of CF_4 can produce *trans*-polyacetylene (*t*-PA), which is similar to the result when the pure O_2 etching takes place, and generate compact needle-tip particles. However, the *t*-PA disappears with the introduction of Cl or H ions. The optimised etching parameters for the needle-like structure formation are as following: Cl_2/O_2 ratio 20% and RF-power (RFP) 100 W, where more compact and even nano-needles are realised with an average etching rate of 2 μm/min. The Cl_2/O_2 plasma etching results indicate that the time-dependent etching mechanism of diamond nano-needles results from (1 1 1) crystal plane selective etching and preferential graphitisation at the twin-plane boundary and dislocation area.

1. Introduction

The emergence of chemical vapor deposition (CVD) techniques for the synthesis of diamond thin films has resulted in overwhelming interest in the use of this material for a wide range of electronic device applications. The focus of most electronic device studies to date has been the fabrication of high-performance power transistor devices, microelectromechanical systems (MEMS), electron field emitting devices, and nitrogen-vacancy center based photonic and quantum devices [1–4]. One of key challenges to fabricate such devices is the ability to control and obtain a specific diamond surface for the subsequent process and application purpose.

Reactive ion etching (RIE) is an effective process for the formation of diamond nanostructures with precise and controllable dimension. Particularly for inductively coupled plasma (ICP)-RIE, it delivers higher etching rate, better uniformity, higher selectivity and lower crystal lattice damage. Pure oxygen plasma has been used to produce diamond micro-mechanical components, whilst the majority of etching processes are based on oxygen plasma in combination with a secondary gas [5,6]. There are a number of reports on the diamond nano-structuring by RIE. Lin et al. have reported the fabrication of nano-needles on ultra-nanocrystalline diamond by RIE [4]. Izak et al. have introduced ICP-RIE to realize the needle-like formation on polycrystalline diamond (PCD) [7]. Practically, the characteristics (e.g. fabricated colour centre or ultra-high elastic deformation) of such needle-like structures offers the new potential for applications, such as single photon sources or strain-mediated nano-mechanical resonators, etc, through optimised design of diamond nanostructure [4,8]. However, there are few reports on the systematic studies of the formation of the nanostructures against auxiliary gas effect and the associated diamond surface evolution process.

Here, the optimisation and mechanism of nano-needle formation on PCD in different gas system were studied. The PCD with large grain size of over 200 um was selected for this study, in order to minimize the influence of grain boundaries.

2. Experiments

The used PCDs $5 \times 5 \times 1\ mm^3$ in size, cut from a 120-mm-diameter free-standing PCD wafer, which was deposited for 200 h at 900 °C with a rate of 7.5 μm/h by a home-built 100 kW DC arc-jet plasma CVD. To ensure the excellent uniformity of the samples, the entire PCD wafers were polished for one week. These samples were treated in boiling mixed acids and then cleaned in acetone and methanol. Dry etching was carried out using an ICP-RIE system (SENTECH/SI-500) with steady coil power of 800 W. Various etching processes and related parameters are summarized in Table 1.

* Corresponding authors.
E-mail addresses: yz516@leicester.ac.uk, nevermorekevin@163.com (Y. Zheng), haitao.ye@leicester.ac.uk (H. Ye), chengmli@mater.ustb.edu.cn (C. Li).

https://doi.org/10.1016/j.matlet.2019.06.079
0167-577X/

Table 1
Diverse ICP-RIE processes and related parameters.

No.	Gas components (%)	RFP (bias)	Etching time (min)	Etched thickness (μm)	Etching rate (μm/min)
PCD1	O_2 = 100	100	5	7	1.4
PCD2	O_2 = 100	100 + 400	5 + 5	–	–
PCD3,4,5	Cl_2/O_2 = 5, 10, 20	100	5	8, 6, 10	1.6, 1.2, 2
PCD6,7,8	CHF_3/O_2 = 5, 10, 20	100	5	4, 11, 18	0.8, 2.2, 3.6
PCD9,10,11	CF_4/O_2 = 5, 10, 20	100	5	6, 17, 7	1.2, 3.4, 1.4
PCD12	Cl_2/O_2 = 10	100	5 + 5 + 5	19	1.3

A scanning electron microscope (SEM-HITACHI-S4800), atomic force microscopy (AFM, ASYLUM-HVA220) were used to observe the morphology. The etching rates, which were in line with the time reported [7], were estimated using ultra-precise profiler measurements (GUANGLU) by testing the thickness before and after etching. Furthermore, the phases were demonstrated via Raman spectroscopy (NANOPHOTO) with a 532 nm excitation wavelength and the crystal orientations of PCDs were investigated by X-ray

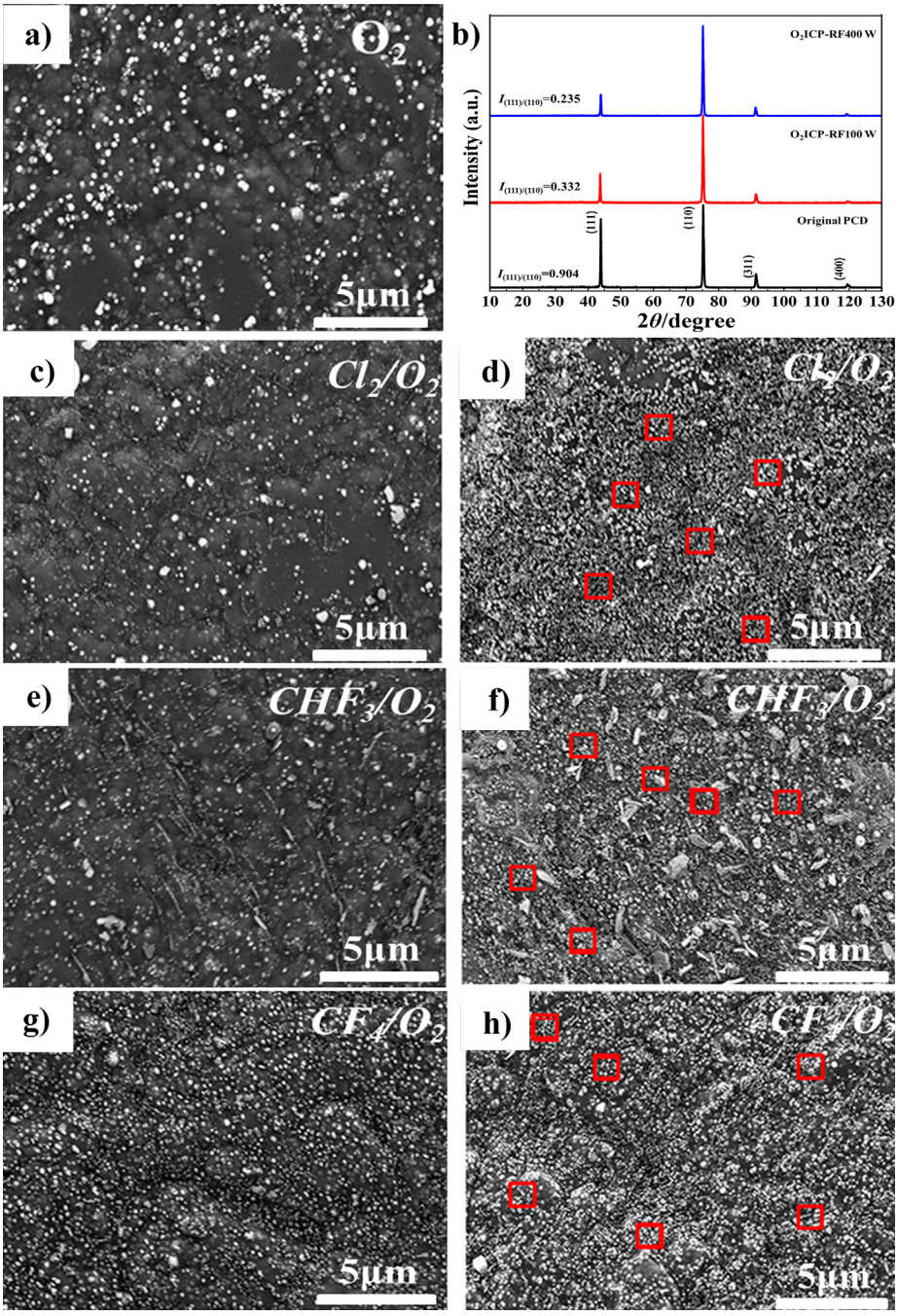

Fig. 1. Surface morphology of etched samples: a) PCD1; c) PCD4; d) PCD5; e) PCD7; f) PCD8; g) PCD10, h) PCD11, and the effect of O_2: b) XRD patterns of multistep etched PCD2.

diffractometer (XRD-Rigaku). Supportively, the surface chemical bonds of the samples were further characterized by X-ray photoelectron spectroscopy (XPS, Thermo Scientific, ESCALAB-250Xi). Before fitting the curves, the spectrum results of XPS were calibrated by the adventitious carbon binding energy [9].

3. Results and discussion

Fig. 1 shows SEM images of various etched PCDs and XRD patterns of the original and pure O_2 etched PCD2. In each 1-μm^2 randomly selected red square area, the number of the nano-needles can be counted statistically via the visible needle tips. In Fig. 1 (d), the average number of needles is approximately 42; whilst this value becomes 27 in Fig. 1(f) and 28 in Fig. 1(h), respectively. Meanwhile, the calculated standard deviations were 9.7%, 32.5%, and 19.1%, respectively. When oxygen was used alone as shown in Fig. 1(a), the diamond surface presented wrinkled and creased morphologies, and nanoscale dots exhibited an uneven distribution with varying sizes. While the oxidation reaction of gas mixture plasma on diamond was related to the etched morphology, the auxiliary gas can also exerted extra effect during surface machining, e.g., etching rate. In Fig. 1(c), several smaller nanoscale dots appeared when the 10% Cl_2 was added during the RIE process. Once 20% of Cl_2 was added, a high volume of compact and homogeneous nano-needles appeared as shown in Fig. 1(d). This was due to the accelerated etching rate (2 μm/min) and enhanced selective etching by higher concentration of Cl. When 10% CHF_3 was added into the RIE chamber, more nano-needle tips appeared with some tendency for alignment as shown in Fig. 1(e). Furthermore, when 20% CHF_3 was added, more nano-needle tips appeared but homogeneity deteriorated, which corresponds to the highest standard deviation of 32.5% described earlier. This was the result of the boosted etching rate (3.6 μm/min), which is likely due to the involvement of the H ions. However, when 10% and 20% of CF_4 were added (instead of CHF_3) to avoid the presence of H ions, as shown in Fig. 1(g) and (h), some more dense and uniform needle-tips formed. Due to the relative faster etching rate (3.4 μm/min), in the 10% CF_4 + O_2 environment, the nano-needles were more apparent and the needle surfaces appeared fresh and sharp-edged. Nevertheless, 20% addition of CF_4 negatively impacted the etching rate (down to 1.4 μm/min). In addition, Fig. 1(b) shows the XRD patterns of the original and O_2 plasma etched PCD2. After etching at RFP of 100 W, $I_{(1\,1\,1)/(1\,1\,0)}$, which is the peak intensity ratio of the (1 1 1) and (1 1 0) orientation, decreases from 0.904 to 0.332. This demonstrates that the (1 1 1) crystal plane of etched PCD exhibits weaker intensity and becomes less dominant in XRD diffraction content after etching. This was due to preferential etching/oxidation of the (1 1 1) orientation compared with other crystal plane, which agrees with existing literature [7,10]. However, after subsequent etching at RFP of 400 W, $I_{(1\,1\,1)/(1\,1\,0)}$ decreases slightly from

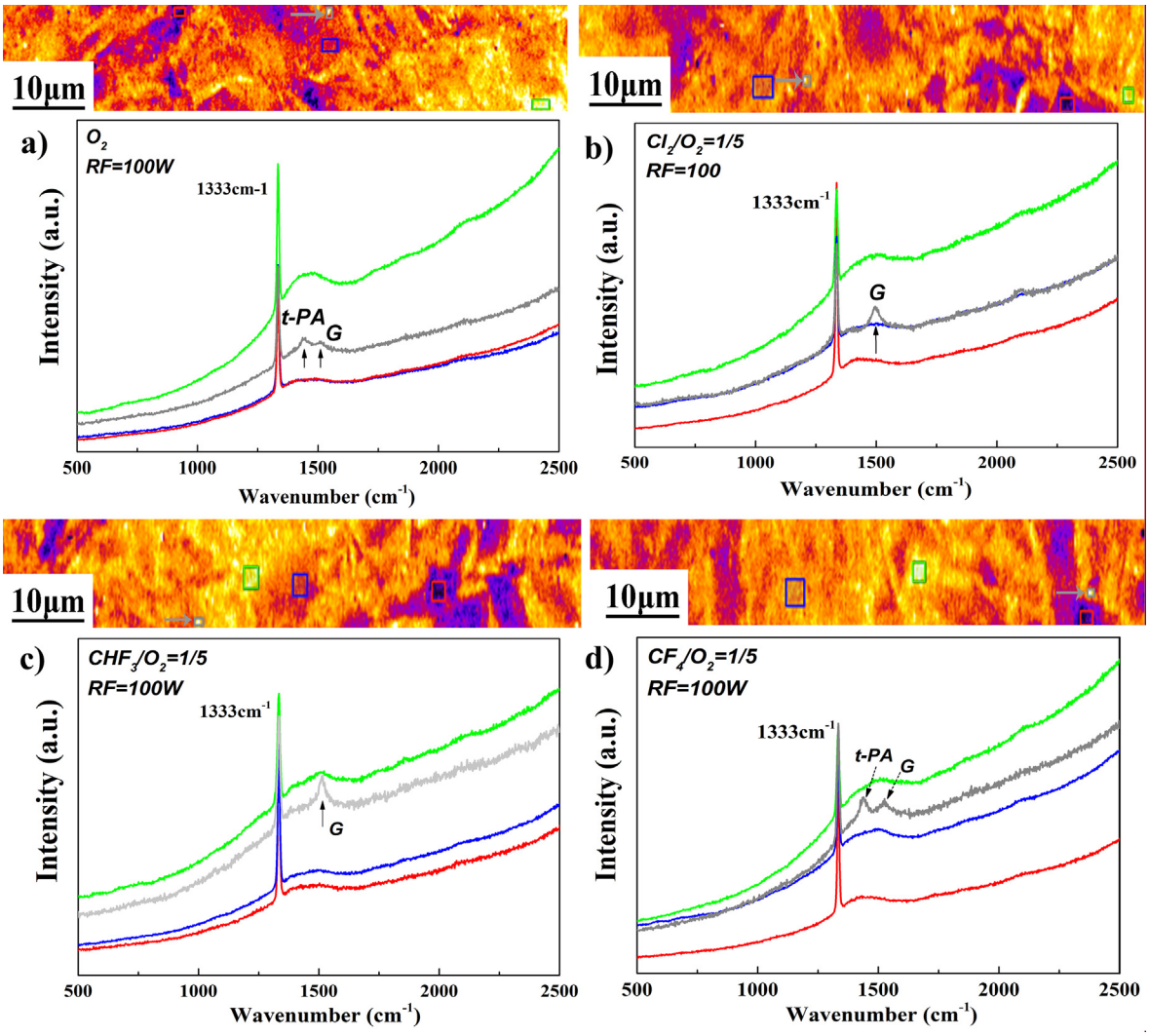

Fig. 2. Raman mapping with different selected areas and corresponding spectra of the etched PCDs: a) PCD1; b) PCD5; c) PCD8; d) PCD11.

0.332 to 0.235. This minor change occurred owing to the dominant role of ion-bombardment enhanced etching when the RFP was as high as 400 W, which surpassed the reactive selective etching on crystal orientations [11].

To investigate the effect of auxiliary gas, we studied Raman spectroscopy on etched PCD samples with the highest additive amount. In Fig. 2, the lines correspond to the same color square marked areas in the mapping pictures. These areas were specially selected from different color regions in the mapping images. We selected the white dots gathered parts of the SEM in mapping pictures, which were the transient state of the needle cluster, in a grey square frame. It should be mentioned that this transient state is the modality during the dynamic formation process from the needle-tip particle emergence to the intact diamond needle formation. In Fig. 2(a) and (d), two distinct peaks of grey spectrum appeared at 1470 and 1580 cm^{-1}, which attribute to the C=C bonds of *trans*-polyacetylene (*t*-PA) and sp^2 graphitic phases, respectively [12]. Thus the addition of CF_4 made no difference on the Raman spectra compared with the samples etched in the pure O_2 (the main gas source) environment. However, in Fig. 2(b) and (c), the disappearance of the 1470 cm^{-1} peaks may be due to the etching effect of Cl and H. This can be interpreted as that the π bond of *t*-PA breaks when the H (or Cl) atoms cover the dangling bonds of the surface C atoms of etched ditches [13]. Furthermore, the peaks of sp^2 graphitic bonds in Fig. 2(c) and (d) were sharper, because of the synergetic oxidation effect of the F element on diamond phase and the self-contained C element. The bulge for the rest of the spectra from 1450 to 1580 cm^{-1} and the obvious background spectra resulted from the disorder or dislocation such as nano-needles and rugged regions where with amorphous carbon. Fig. 2(b) illustrates that these four coloured lines are almost identical, indicating that the etched diamond quality in different regions is the same. Combining with SEM images, the optimal nano-needle formation recipe is the addition of 20% of Cl_2 into O_2. Meanwhile, Fig. 3 shows the deconvoluted high-resolution XPS spectra of PCD1, which etched in the pure O_2 plasma environment. It is observed that the C 1s peak can be mainly deconvoluted into four components at 284.6, 285.5, 286.2 and 288.1 eV, which are attributed to sp^2 graphitic phases, sp^3 diamond phase, C—O and C=O bonds, respectively [12–14]. It should be noted that in the C1s core-energy level spectrum of sample, a shoulder peak at about 289 eV is related to π-π^* bonds and considered as the characteristic of the C=C bonds of *t*-PA, which is shown by the Raman assignment at 1470 cm^{-1} in Fig. 2(a) (it also be the same to this peak in Fig. 2(d)) [12,13]. Furthermore, the deconvoluted O 1s peaks at 532.4 and 533.9 eV are attributed to the O=C and C—O—C bonds of sp^2 graphite, respectively, which was generated from oxidation (reactive etching) of diamond surface [14].

Besides the selective etching of different crystal orientations, preferential etching of the dislocation and boundary area also plays an important role in the diamond-needle formation. Fig. 4 presents the nano-needle formation mechanism with the Cl addition at a small flow rate, at which PCD was etched slower than the optimized process so that the step-by-step investigation was presented

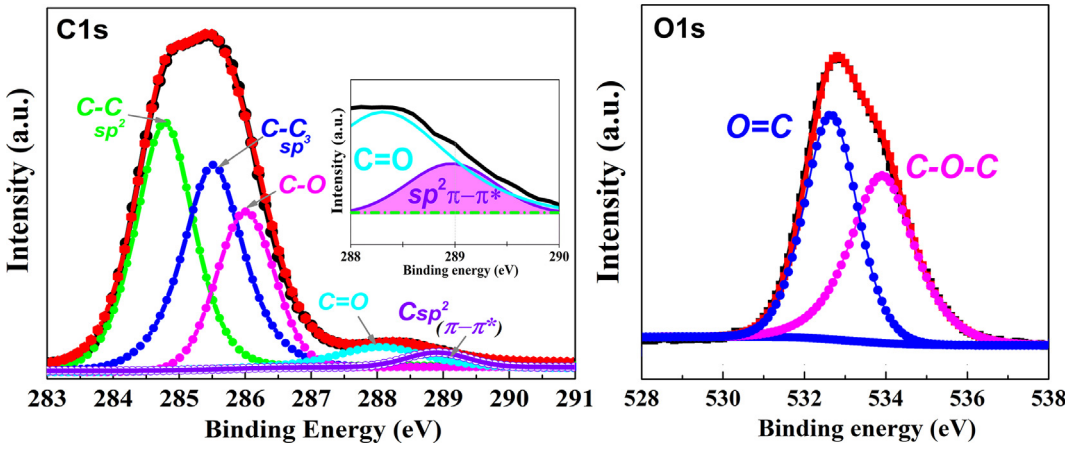

Fig. 3. Fine fitted C 1s and O 1s XPS spectra of etched surface of PCD1. The inset is the amplified XPS shoulder peak assignment of π-π^* bonds.

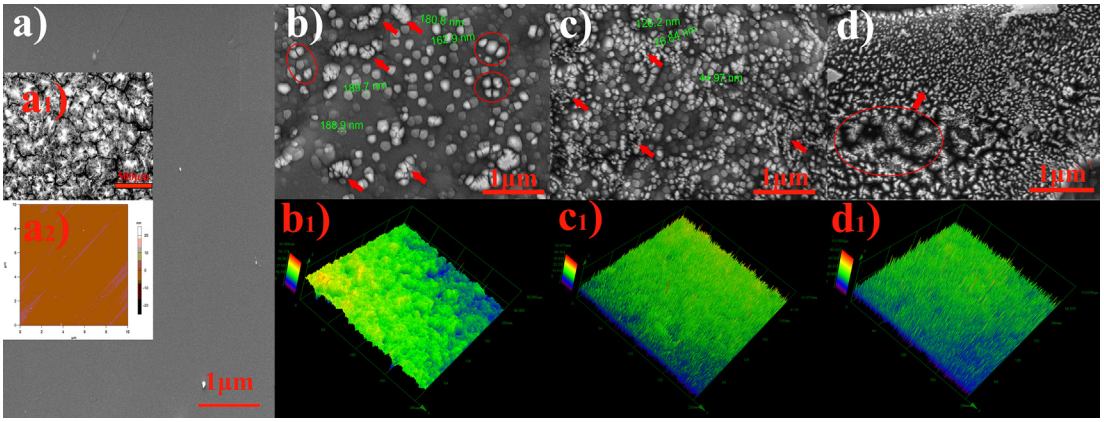

Fig. 4. Surface morphology of original PCD and time-dependent etching results: a) SEM, a_1) OM, a_2) AFM images of as-polished original PCD12; SEM and 3D-AFM images of PCD12 etched for different duration: b) and b_1) of 5 mins; c) and c_1) of 10 mins; d) and d_1) of 15 mins.

easily. A smooth surface (RMS: 1.59 nm) of as-polished PCD was shown with light-scratches and grain size larger than 200 μm in Fig. 4(a, $a_{1\text{-}2}$). These large grains can act as a homogeneous unit. After 5 min etching, in Fig. 4(b), the cauliflower-like morphologies can be seen, which consist of some smaller pieces and etched boundary. Meanwhile, the preferential etching of the dislocation area and the twin boundary revealed a sand grain-shaped particle, twin, four-leaf clover and cauliflower shapes among some of the slowly etched parts (200–500 nm). This indicates a nano-needle transient state in which the twin boundary and the planar defects were etched preferentially in addition to the etchings on the cauliflower-shaped parts. The nano-needles originate from these parts and undergo further etching. During this process, the nearby regions also generate new particles and the process continues. This phenomenon is demonstrated in Fig. 4(c), which shows much more compact needles (the width is less than 50 nm). When the etching time was extended to 15 min, as shown in Fig. 4(d), many more even and tiny nano-needles (the width is less than 10 nm) appeared. From the fine perspective of 3D images and automatic calculation results of average height shown in Fig. 4(b_1, c_1, d_1), the sample surface changed from its initial rugged features to the newly generated needles with statistical mean length (SML) of 41.54 nm and then to the full-fledged nano-needles with SML of 56.52 nm. Consequently, the average high aspect ratio (large than 5:1) of the nano-needles was obtained.

4. Conclusion

The evolution of the needle-like structure formation by ICP-RIE on free-standing PCDs, were investigated using step-by-step morphology deduction and phase analysis. The CF_4/O_2 plasma can produce the compact needle-tip particles and generate the chemical bonds associated with *trans*-polyacetylene. However, both adding Cl_2 and CHF_3 in O_2 plasma can destroy the *trans*-polyacetylene. An optimised process condition for obtaining more compact and uniform nano-needle structure is to use Cl_2/O_2 = 20% plasma, and RFP of 100 W with a resultant etching rate of 2 μm/min. The physical mechanism associated with the observed phenomenon can be explained by the time-dependent etching of diamond nano-needles under low plasma power where the synergetic effect between the crystal orientation selective etching and the preferential oxidation at the twin-plane boundary and dislocation regions plays a dominant role.

Declaration of Competing Interest

None.

Acknowledgments

This work was supported by the National Key Research and Development Program of China (no. 2016YFE0133200) and the European Union's Horizon-2020 Research program (no. 734578). Special thanks to the national high-level university-sponsored graduate program of China Scholarship Council (CSC).

References

[1] S. Shikata, Single crystal diamond wafers for high power electronics, Diam. Relat. Mater. 65 (2016) 168–175, https://doi.org/10.1016/j.diamond.2016.03.013.
[2] J. Isberg, J. Hammersberg, E. Johansson, T. Wikström, D.J. Twitchen, A.J. Whitehead, S.E. Coe, G.A. Scarsbrook, High carrier mobility in single-crystal plasma-deposited diamond, Science 297 (2002) 1670, https://doi.org/10.1126/science.1074374.
[3] R.S. Sussmann, CVD Diamond for Electronic Devices and Sensors, John Wiley & Sons, 2009.
[4] S. Kunuku, K.J. Sankaran, C.Y. Tsai, W.H. Chang, N.H. Tai, K.C. Leou, I.N. Lin, Investigations on diamond nanostructuring of different morphologies by the reactive ion etching process and their potential applications, ACS. Appl. Mater. Interfaces 15 (2013) 7439–7449, https://doi.org/10.1021/am401753h.
[5] Y. Tao, C.L. Degen, Single-crystal diamond nanowire tips for ultrasensitive force microscopy, Nano. Lett. 15 (2015) 7893–7897, https://doi.org/10.1021/acs.nanolett.5b02885.
[6] A. Toros, M. Kiss, T. Graziosi, H. Sattari, P. Gallo, N. Quack, Precision micro-mechanical components in single crystal diamond by deep reactive ion etching, Microsyst. Nanoeng. 12 (2018) 1–8, https://doi.org/10.1038/s41378-018-0014-5.
[7] T. Izak, A. Kromka, O. Babchenko, M. Ledinskya, K. Hruska, E. Verveniotis, Comparative study on dry etching of polycrystalline diamond thin films, Vacuum 86 (2012) 799–802, https://doi.org/10.1016/j.vacuum.2011.07.023.
[8] A. Banerjee, D. Bernoulli, H. Zhang, M.F. Yuen, J.B. Liu, J.C. Dong, F. Ding, J. Lu, M. Dao, W.J. Zhang, Y. Lu, S. Suresh, Ultra-large elastic deformation of nanoscale diamond, Science 360 (2018) 300–302, https://doi.org/10.1126/science.aar4165.
[9] B.V. Crist, XPS in industry—problems with binding energies in journals and binding energy databases, J. Electron. Spectrosc. Relat. Phenom. 231 (2019) 75–87, https://doi.org/10.1016/j.elspec.2018.02.005.
[10] C.Q. Sun, H. Xie, H.T. Ye, P. Hing, Preferential oxidation of diamond {111}, J. Phys. D: Appl. Phys. 33 (2000) 2196–2199, https://doi.org/10.1088/0022-3727/33/17/316.
[11] M.J. Jackson, W. Ahmed, Micro and Nano-manufacturing, vol. II, Springer, 2018.
[12] X.J. Hu, C.K. Chen, S.H. Lu, High mobility n-type conductive ultra-nanocrystalline diamond and graphene nanoribbon hybridized carbon films, Carbon 98 (2016) 671–680, https://doi.org/10.1016/j.carbon.2015.11.057.
[13] S.J. Sque, R. Jones, P.R. Briddon, Structure, electronics, and interaction of hydrogen and oxygen on diamond surfaces, Phys. Rev. B 73 (2006), https://doi.org/10.1103/PhysRevB.73.085313 085313.
[14] R.A. Gaashani, A. Najjar, Y. Zakaria, S. Mansoura, M.A. Atieha, XPS and structural studies of high quality graphene oxide and reduced graphene oxide prepared by different chemical oxidation methods, Cream. Int. 45 (2019) 14439–14448, https://doi.org/10.1016/j.ceramint.2019.04.165.